Transverse Signal Decay Under the Weak Field Approximation: Theory and Validation

Avery J.L. Berman[1,2] and G. Bruce Pike[1,2,3]

Purpose: To derive an expression for the transverse signal time course from systems in the motional narrowing regime, such as water diffusing in blood. This was validated in silico and experimentally with ex vivo blood samples.
Methods: A closed-form solution (CFS) for transverse signal decay under any train of refocusing pulses was derived using the weak field approximation. The CFS was validated via simulations of water molecules diffusing in the presence of spherical perturbers, with a range of sizes and under various pulse sequences. The CFS was compared with more conventional fits assuming monoexponential decay, including chemical exchange, using ex vivo blood Carr-Purcell-Meiboom-Gill data.
Results: From simulations, the CFS was shown to be valid in the motional narrowing regime and partially into the intermediate dephasing regime, with increased accuracy with increasing Carr-Purcell-Meiboom-Gill refocusing rate. In theoretical calculations of the CFS, fitting for the transverse relaxation rate (R_2) gave excellent agreement with the weak field approximation expression for R_2 for Carr-Purcell-Meiboom-Gill sequences, but diverged for free induction decay. These same results were confirmed in the ex vivo analysis.
Conclusion: Transverse signal decay in the motional narrowing regime can be accurately described analytically. This theory has applications in areas such as tissue iron imaging, relaxometry of blood, and contrast agent imaging. **Magn Reson Med 80:341–350, 2018. © 2017 International Society for Magnetic Resonance in Medicine.**

Key words: transverse relaxation; CPMG; magnetic inhomogeneities; blood; diffusion

INTRODUCTION

Understanding the detailed nature of transverse signal decay in the presence of magnetic perturbations plays an important role in many fields of MRI: from deriving baseline physiological parameters related to the blood oxygenation level–dependent signal (1) to quantifying structural properties of bone (2). In the presence of magnetic perturbers, it is well known that the observed T_2 or

[1]Department of Biomedical Engineering, McGill University, Montreal, Quebec, Canada.

[2]Hotchkiss Brain Institute, University of Calgary, Calgary, Alberta, Canada.

[3]Departments of Radiology and Clinical Neurosciences, University of Calgary, Calgary, Alberta, Canada.

*Correspondence to: Avery Berman, Ph.D., Health Science Centre, room 2910E, 3330 Hospital Drive NW, Calgary, AB, Canada T2N 4N1.
E-mail: avery.berman@mail.mcgill.ca

T_2^* relaxation times depend on several factors, such as the perturbation magnitude (i.e., field strength and magnetic susceptibility offset between the perturbers and the surrounding medium), the interplay between molecular diffusion and the spatial scale of the perturbers, and the refocusing rate in a multi-echo spin-echo (SE) sequence (3,4). Depending on the combination of these parameters, the system is said to be in one of three dephasing regimes: static dephasing, motional narrowing, or an intermediate dephasing regime, with each regime displaying unique signal characteristics.

For red blood cells (RBCs) in blood, the shape and size of the cells and the diffusion coefficient of blood water have relatively low variability, such that the system exists in the motional narrowing regime. In this regime, the characteristic time for a water molecule to diffuse the length of a perturber is much less than the time for a spin at the surface of a perturber to dephase (5). Using an algebraic approximation for the temporal correlation function, referred to as the weak field approximation (WFA), Jensen and Chandra (6) derived an expression for how the transverse signal decay rate would change (ΔR_2) in a random distribution of perturbers as a function of the refocusing interval in a Carr-Purcell-Meiboom-Gill (CPMG) acquisition. Following an alternative approach known as the Gaussian phase approximation, Sukstanskii and Yablonskiy (5) derived a closed-form solution for how the transverse signal would evolve during free induction decay (FID) and as a function of SE time in a single SE-type measurement. This derivation resulted in the same ΔR_2 as in the FID limit for spheres from the weak field approximation.

The WFA has successfully been applied to model CPMG relaxometry results from ex vivo blood samples (6–9) and in vivo tissue non-heme iron depositions (6,10) using its predictions of ΔR_2 to make inferences on the underlying physiology. However, with the increasing use of SE-based pulse sequences that sample away from the spin echo itself, such as asymmetric spin echo (11), gradient echo sampling of the spin echo (12), and gradient echo sampling of FID and echo (13), it is important to be able to compare the measurements with the entire predicted time course, rather than solely the signal observed at the spin echoes. Here we present a closed-form solution (CFS) describing the complete transverse signal time course for an arbitrary number of refocusing pulses using the weak field approximation. The validity of the CFS was examined using simulations from distributions of spheres over a range of perturber radii and pulse sequences, in which the predictions of the CFS could be compared with the known ground truth of the simulations. Finally, fitting using the CFS was

experimentally compared with two monoexponential models for ΔR_2, including chemical exchange, using CPMG SE data from ex vivo human blood samples at 3 T.

THEORY

Following the derivation of the WFA from Jensen and Chandra (6), for a system of hydrogen nuclei subjected to a spatially varying magnetic field, the total field along the longitudinal direction at a point $\boldsymbol{r}$ is given by the sum of the main magnetic field, B_0, and an inhomogeneous component, $\Delta B(\boldsymbol{r})$. The spatial variation of this field can be described by an average over the inhomogeneous component for all pairs of points, $\boldsymbol{r}$ and $\boldsymbol{r}'$, referred to as the spatial correlation function

$$C(\boldsymbol{r} - \boldsymbol{r}') = \Delta B(\boldsymbol{r})\Delta B(\boldsymbol{r}')_{\text{fld}} \qquad [1]$$

Because of the molecular diffusion through the field over time, C will effectively vary over a time interval Δt and is described by the temporal correlation function, $K(\Delta t)$, as

$$\begin{aligned} K(|\Delta t|) &= \Delta B[\boldsymbol{r}(t)] \ \Delta B[\boldsymbol{r}(t + \Delta t)]_{\text{fld+diff}} \\ &= C[\boldsymbol{r}(t)] - C[\boldsymbol{r}(t + \Delta t)]_{\text{diff}}, \end{aligned} \qquad [2]$$

where the average is over space and all possible diffusion trajectories.

For a system of spins in the motional narrowing regime, diffusion across the field inhomogeneities reduces the transverse signal magnitude, $S'(t)$, at time t during a CPMG experiment as (5,6)

$$S'(t) = \exp\left\{ -\frac{\gamma^2}{2} \int_0^t d\tau \int_0^t d\tau' \sigma(\tau)\sigma(\tau')K(|\tau - \tau'|) \right\}, \qquad [3]$$

where $\sigma(t)$ is a spin flip function of magnitude 1 and changes sign upon application of any 180° refocusing pulses.

Although analytic expressions for $K(t)$ for systems of spheres and infinite cylinders exist (5,6), deriving an exact expression for $K(t)$ is generally only tractable for simple geometries. A relatively simple form can be derived by considering the angular average of $C(\boldsymbol{r})$ and assuming it decays monotonically toward 0 as $r \rightarrow \infty$. By assuming that this radial correlation function, $G(r)$, decays as a quadratic exponential, i.e.,

$$G(r) = \frac{1}{4\pi}\int_0^\pi d\theta \int_0^{2\pi} d\phi \sin\theta C(r, \theta, \phi) = G_0 e^{-(r/r_c)^2}, \qquad [4]$$

where $G_0 = C(0)$ is the mean square field inhomogeneity and r_c is a characteristic length that depends on the exact description of the perturbers, then, for unrestricted and isotropic diffusion in three dimensions, $K(t)$ will take the algebraic form (6)

$$K(t) = G_0\left(1 + \frac{4Dt}{r_c^2}\right)^{-\frac{3}{2}}, \qquad [5]$$

where D is the diffusion coefficient of water. This derivation assumes that the object is finite in three dimensions, or more practically, that the field changes quickly relative to diffusion along any direction. Therefore, it cannot describe the correlation function for long cylinders, which are frequently used to model blood vessels, or broad disks. Using Equation [5] and assuming that $S'(t)$ decays monoexponentially as $t \rightarrow \infty$, an asymptotic solution for ΔR_2 is (6)

$$\Delta R_2 = G_0 \frac{\gamma^2 r_c^2}{2D} F\left(\frac{2D\tau_{180}}{r_c^2}\right), \qquad [6]$$

where F is defined by Equation [30] in (6) and τ_{180} is the CPMG refocusing interval.

Using the correlation function in Equation [5], it is also possible to explicitly solve the integral in Equation [3] to produce a CFS for the signal magnitude at any time, t. If no refocusing pulses are applied, then the solution of this integral gives the FID signal

$$S'(t) = \exp\left\{ -\frac{\gamma^2}{2} G_0\tau_D^2 \times \left[\frac{t}{\tau_D} - \left(\frac{1}{4} + \frac{t}{\tau_D}\right)^{\frac{1}{2}} + \frac{1}{2} \right] \right\}, \qquad [7]$$

where $\tau_D \equiv r_c^2/D$ is a characteristic diffusion time. In the case of a SE or CPMG sequence, this equation holds for $t < {}^1\!/_2 \ \tau_{180}$. This and the following expression were recently independently derived (14). After one refocusing pulse, we get

$$\begin{aligned} S'(t) =\exp\Bigg\{ &-\frac{\gamma^2}{2} G_0\tau_D^2 \times \Bigg[\frac{t}{\tau_D} + \left(\frac{1}{4} + \frac{t}{\tau_D}\right)^{\frac{1}{2}} \\ &+ \frac{3}{2} - 2\left(\frac{1}{4} + \frac{t - \tau_{180}/2}{\tau_D}\right)^{\frac{1}{2}} - 2\left(\frac{1}{4} + \frac{\tau_{180}/2}{\tau_D}\right)^{\frac{1}{2}} \Bigg] \Bigg\}, \end{aligned} \qquad [8]$$

where $t > {}^1\!/_2 \ \tau_{180}$ if only one refocusing pulse is applied or ${}^1\!/_2 \ \tau_{180} < t < {}^3\!/_2 \ \tau_{180}$ if another pulse is applied at $t = {}^3\!/_2 \ \tau_{180}$. Continuing in this manner, the CFS after N refocusing pulses can be deduced (15) as

$$\begin{aligned} S'(t) = \exp\Bigg\{ &-\frac{\gamma^2}{2} G_0\tau_D^2 \\ \times\Bigg[&\frac{t}{\tau_D} + (-1)^{N+1}\left(\frac{1}{4} + \frac{t}{\tau_D}\right)^{\frac{1}{2}} + \frac{1}{2} + N \\ &+ \sum_{n=1}^N 2(-1)^{N-n+1}\left(\frac{1}{4} + \frac{t - (2n-1)\tau_{180}/2}{\tau_D}\right)^{\frac{1}{2}} \\ &+ 2(-1)^n\left(\frac{1}{4} + \frac{(2n-1)\tau_{180}/2}{\tau_D}\right)^{\frac{1}{2}} + 4(-1)^n(N-n)\left(\frac{1}{4} + \frac{n\tau_{180}}{\tau_D}\right)^{\frac{1}{2}} \Bigg] \Bigg\} \end{aligned} \qquad [9]$$

This expression holds even if no more pulses are applied after the Nth refocusing pulse, and the system proceeds to evolve freely as an FID.

METHODS

The evaluation of the CFS in Equation [9] was implemented in MATLAB R2015a (MathWorks, Natick, MA,

USA) using a function handle that was updated at each refocusing pulse and that iteratively added the terms in the summation to itself up to the *N*th pulse.

Simulations

As written, Equation [9] represents a solution for transverse signal decay that could apply to a variety of systems, given appropriate values for r_c and G_0 and that the conditions of the WFA are satisfied. To assess the validity of the CFS with concrete values, spherical perturbers were considered, for which r_c and G_0 are known. For spheres of radius R and with a susceptibility offset $(\Delta\chi)$ relative to the external medium, r_c and G_0 are (5,6,16)

$$r_c = \left(\frac{4}{3\sqrt{\pi}}\right)^{\frac{1}{3}} R, \qquad [10]$$

and

$$G_0 = \frac{4}{45}\zeta(1-\zeta)(\Delta\chi B_0)^2, \qquad [11]$$

where ζ is the volume fraction occupied by the spheres, and $\Delta\chi$ is in SI units. The original derivation of the WFA assumed that the positions of the perturbers were uncorrelated, which allowed for the possibility of overlapping perturbers, but the $(1 - \zeta)$ correction factor in G_0 was added to account for this with nonoverlapping perturbers (16). The true geometry of perturbers like RBCs or iron depositions would result in different values for r_c that may not be readily calculated analytically. This is examined in more detail in the Supporting Information, where the temporal correlation function from the WFA is compared with the exact correlation function of the Gaussian phase approximation for multiple spheroid geometries (see Supporting Fig. S1).

The accuracy of the CFS was compared with simulations of the transverse MR signal from distributions of randomly positioned spheres using MATLAB. The simulations were performed using the deterministic diffusion method in three dimensions (17). This is a computationally efficient simulation technique, and it inherently models the perturber boundaries as freely permeable, as required by the WFA. This method spatially discretizes the volume over which the simulation is run onto a lattice and, for a given distribution of perturbers, calculates the field offsets generated by them over this lattice. Following a 90° excitation pulse, each element of the lattice has a uniform transverse magnetization with an initial phase of 0 and magnitude of 1. In time steps, δt, the transverse magnetization at the (k,l,m)th lattice element, M_{klm}, precesses by an angle $\Delta\phi_{klm} = \gamma\ \Delta B_{klm}\ \delta t$, where ΔB_{klm} is the field offset at that lattice element. Diffusion is modeled by an isotropic, Gaussian blurring of the magnetization along each dimension independently. This was implemented by linear convolution of the magnetization with the 1-dimensional discrete diffusion kernel with a width parameter equal to the expected mean-square displacement of water molecules, $\sigma^2 = 2D\delta t$ (18). Together, the magnetization at the *N*th time point can be summarized by

$$\mathbf{M}_n = \begin{cases} \mathbf{M}_{n-1} \cdot e^{-\Delta\mathbf{\Phi}} \otimes \mathbf{D} & n > 0 \\ 1 & n = 0 \end{cases}, \qquad [12]$$

where $\Delta\mathbf{\Phi}$ is the precession matrix, $\mathbf{D}$ is the diffusion matrix, $\mathbf{1}$ is a matrix consisting of all ones, $\cdot$ denotes element-wise multiplication, and $\otimes$ denotes convolution. Refocusing pulses were modeled by taking the complex conjugate of the magnetization at each lattice element. Finally, the signal magnitude at the *N*th time point is given by

$$S_n = \frac{1}{N^3}\left|\sum_{k,l,m} M_{klm,n}\right|, \qquad [13]$$

where N is the number of lattice elements summed along each dimension, and the sum was only performed over the central one-third of the lattice width along each dimension, to avoid convolution edge effects.

The field offsets generated by each sphere were given by

$$\Delta B(r) = \begin{cases} \frac{1}{3}\Delta\chi B_0\left(\frac{R}{r}\right)^3(3\cos^2\theta - 1) & r > R \\ 0 & r \leq R \end{cases}, \qquad [14]$$

where θ is the angle between B_0 and the line joining the center of a sphere and a point a distance r from the sphere center. The field offsets for each sphere were independently calculated and summed across the lattice to give ΔB_{klm}.

To evaluate the validity of the CFS across dephasing regimes, the simulations were run on populations of spheres whose radii were increased from 0.9 up to 24 μm with ζ held constant at 3%, for which sphere overlap was negligible. $\Delta\chi$ of the spheres was set to 1.2 ppm, which is equivalent to the susceptibility offset between 60% oxygenated RBCs and plasma (19,20), and would also approximately give the same G_0 from iron depositions in deep gray matter (6). Other settings included $B_0 = 3$ T, $\delta t = 0.25$ ms, total simulation time $= 80$ ms, $D = 1.0\ \mu m^2/ms$, and intrinsic T_2 relaxation was ignored. Under these settings, the parameter typically used to classify the dephasing regime, $\alpha = \tau_D\delta\omega = r_c^2/D\gamma\Delta\chi B_0/3$, varies from 0.22 to 153, where $\alpha \ll 1$ defines the motional narrowing regime; $\alpha \gg 1$ defines the static dephasing regime; and $\alpha \sim 1$ represents the intermediate regime. For simulations in which the sphere radius was less than 5 μm, the time step needed to be decreased to 0.05 ms to properly sample the diffusion effects in the field offsets around the perturbers; for larger radii, time steps less than 0.25 ms negligibly affected the simulations.

Simulated pulse sequences included FID, SE (echo time $= 80$ ms), and CPMG using $\tau_{180} = 40$ or 10 ms, resulting in two or eight echoes, respectively. These simulations were performed on 10 randomly seeded distributions of 0.9-μm-radius spheres on a 600^3 lattice with a side length of 90 μm isotropic. These distributions were reused for the larger radii by assigning them an effective lattice size of $90 \times R/0.9$ μm.

Analysis

Before comparing the simulations with the CFS in Equation [9], the simulations were averaged across all random
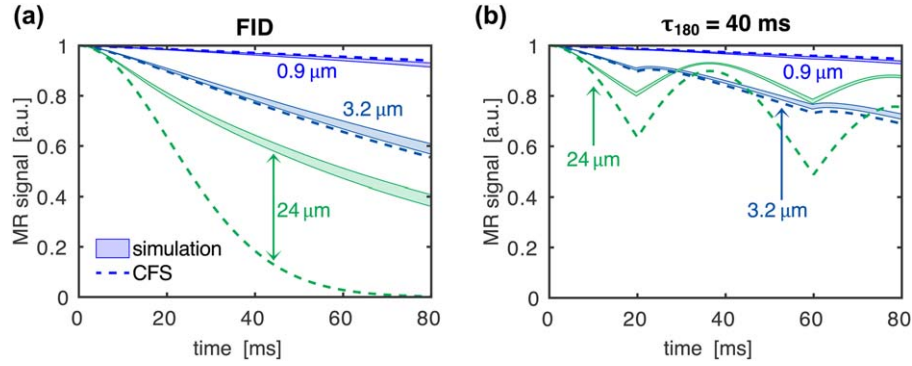
FIG. 1. Comparison of the mean simulated free induction decay (FID) (**a**) and Carr-Purcell-Meiboom-Gill (CPMG) (**b**) signals versus the CFS for select sphere radii. The shaded bands represent the mean ± standard deviation of the simulated signals, and the dashed lines represent the closed-form solution (CFS) for each radius.

distributions for each set of run parameters (e.g., radius, τ_{180}). Each set of signals was compared by examining the root mean square error between the time series and ΔR_2. ΔR_2 was calculated at the final time point, echo time (TE) = 80 ms, using $\Delta R_2 = -\ln(S)/\text{TE}$.

Ex Vivo Validation

The CFS was fit to previously published ex vivo human blood CPMG data collected at 3 T (7). Across 40 blood samples from 10 subjects, the blood oxygen saturation (SO$_2$) varied between 20 and 98%, and hematocrit varied between 39 and 48%. Samples were scanned at room temperature using a T$_2$-prepared segmented echo-planar imaging sequence with τ_{180} values of 2, 2.5, 3, 3.5, 4, 5, 6, 8, 10, 12.5, 17.5, 27.5, and 37.5 ms. For each refocusing interval, six different T$_2$ preparation durations were used, resulting in six different effective TEs. Because of the presence of image artifacts in some data sets, one subject's samples were excluded and an additional five samples from four other subjects were excluded, resulting in 31 samples being analyzed.

An analysis of these data, which evaluated the relationships among G_0, blood oxygenation, and additional blood parameters, has already been performed (7); the objective, here, was to evaluate the ability of the CFS to fit the relaxometry data in comparison with more conventional models of transverse relaxation. Therefore, three different models were fit to the data for each subject using an expression of the form

$$S_{ij}(\text{TE}) = S_{0_{ij}}\exp(-R_{2,0_i}\text{TE})S'(\text{TE}, \tau_{180_j}, G_{0_i}, \tau_D), \quad [15]$$

where i is the blood sample index; j is the τ_{180} index; $S_{ij}(\text{TE})$ is the mean measured signal intensity at TE for the jth refocusing interval of the ith sample; $S_{0_{ij}}$ is the initial signal intensity for the jth refocusing interval of the ith sample; $R_{2,0_i}$ is the intrinsic R_2 of the ith sample; G_{0_i} is the mean square field inhomogeneity of the ith sample; $\tau_D = r_c^2/D$ was constrained to be constant across all samples for a given subject; and S' was dependent on the model. In the first model, referred to as "WFA-CFS," S' was the CFS in Equation [9]. In the second and third models, S' was given by $\exp(-\Delta R_{2_{ij}}\text{TE})$. In the second model, referred to as "WFA-R_2," $\Delta R_{2_{ij}} = \Delta R_2(\tau_{180_j}, G_{0_i}, \tau_D)$, as defined in

Equation [6], the monoexponential expression from Jensen and Chandra (6). In the third model, referred to as "LM-R_2," the Luz-Meiboom exchange model of relaxation was used with (21)

$$\Delta R_{2_{ij}} = K_{0_i}\tau_{ex}\left(1 - \frac{2\tau_{ex}}{\tau_{180_j}}\tanh\left(\frac{\tau_{ex}}{2\tau_{180_j}}\right)\right), \quad [16]$$

in which G_{0_i} was replaced by K_{0_i}, the characteristic square field inhomogeneity of the ith sample; and τ_D was replaced by τ_{ex}, the water exchange time, which was constrained to be constant across all samples for a given subject. All three models were fit in the signal space, as this allowed for their quality of fit (sum of square residuals) to be quantitatively compared. For each subject, therefore, each model resulted in 52 estimates of $S_{0_{ij}}$ (one per vial and τ_{180}), four estimates of $R_{2,0_i}$ and G_{0_i} or K_{0_i} (one per vial), and one estimate of τ_D or τ_{ex} (one per subject).

For all models, echo times from a given sample were excluded if the mean image intensities were less than two standard deviations above the mean background intensity, and all echoes from a given τ_{180} were excluded if less than three echoes passed this criterion. All fits used the MATLAB function lsqcurvefit with the trust-region-reflective algorithm, with T$_{2,0_i}$ (1/R$_{2,0_i}$) bounded between 10^{-6} and 300 ms, $G_{0_i} \geq 0$, $\tau_D \geq 0$, $K_{0_i} \geq 0$, and $\tau_{ex} \geq 0$. Samples in which the fitted T$_{2,0}$ were within 1% of the upper bound were deemed failed fits and were excluded from further analyses. These failed fits tended to correlate with cases of excessive ghosting, resulting from residual motion of the blood in the syringes.

RESULTS

Validation of the Closed-Form Solution

Figure 1 compares the simulated FID and $\tau_{180} = 40$ ms time series against the CFS for several radii. The agreement between simulation and CFS was close for the 0.9-μm radius, whereas for the 24-μm radius, the CFS significantly overestimated the decay. At the 3.2-μm radius, the agreement was also close, but the decay was slightly overestimated by the CFS. These three radii demonstrate the transition from the motional narrowing regime to the
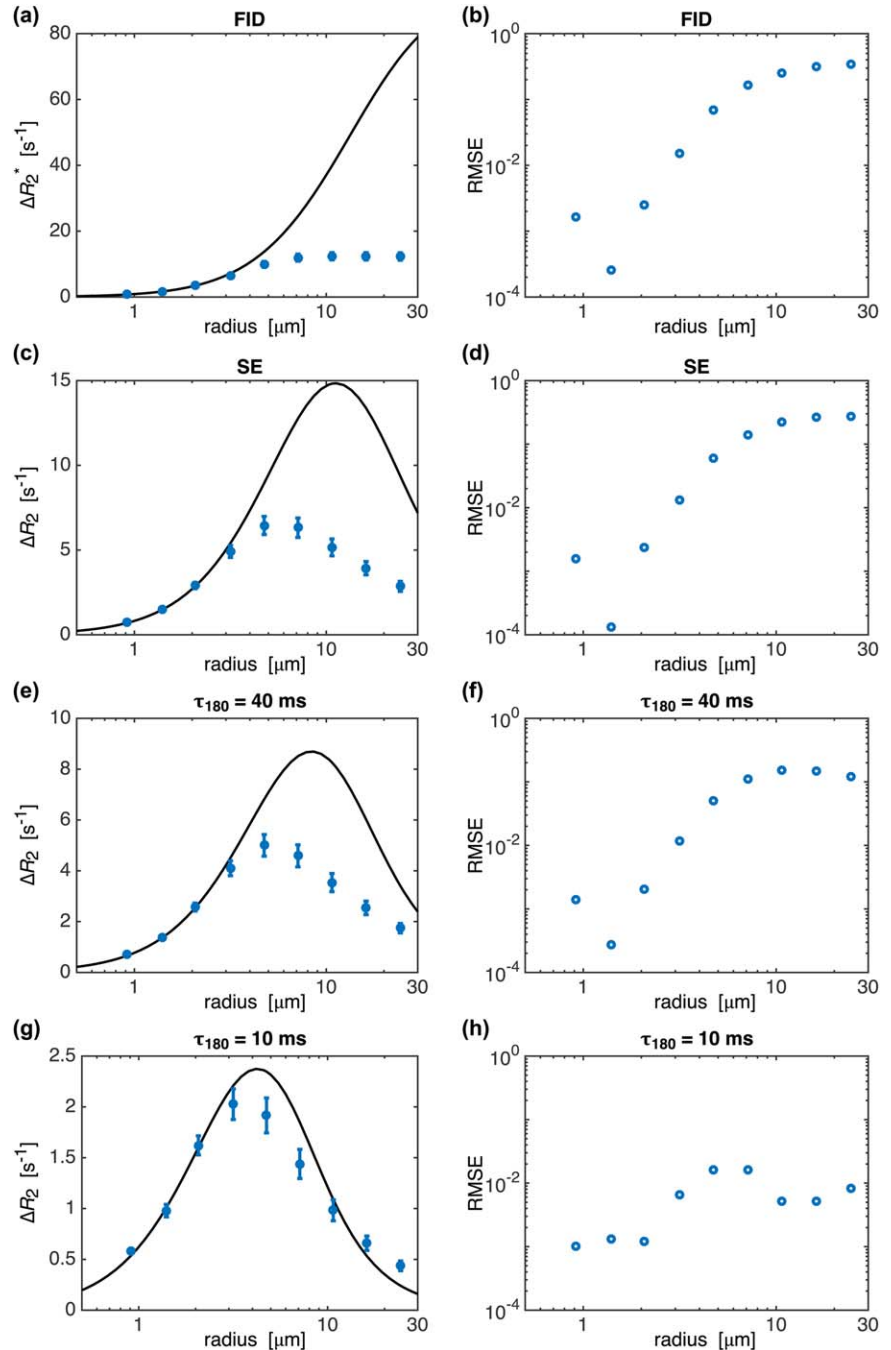
FIG. 2. Accuracy of the CFS versus simulations across a range of sphere radii and for FID, spin echo, and two CPMG pulse sequences. Left: Comparison of $\Delta R_2^{(*)}$ from the simulations (circle markers) with the predicted values from the CFS (black line). The error bars represent the standard deviation of the mean simulated values. Right: Root mean square error across time between the mean simulations and the CFS. Note that the ΔR_2 scales change between the pulse sequences' figures, whereas they are constant for the root mean square errors. SE, spin echo; RMSE, root mean square error

static dephasing regime. Figure 2, which compares ΔR_2 with the root mean square error between the simulations and the CFS, shows this transition more continuously. As τ_{180} decreased, the accuracy of the CFS increased until the differences were negligible for all radii at $\tau_{180} = 10$ ms. To consider the signal from tissue with a given perturber radius, R, but another diffusion coefficient, D, the results from an effective perturber radius $R' = R \times (1\,\mu m^2/ms/D)^{1/2}$ can be used (22).

Closed-Form Solution Versus Monoexponential Decay

Examples of the CFS for multiple refocusing intervals are shown in Figure 3 and are plotted along with the monoexponential decay described by Equation [6]. These curves were generated using spheres to approximate RBCs with $\zeta = 40\%$, radius $= 3\,\mu m$, $SO_2 = 60\%$, $B_0 = 3$ T, and assuming $D = 2.0\,\mu m^2/ms$ at $37\,^\circ C$ (6,23). Figure 3b shows an enlargement of the CFS and the monoexponential curve for the case $\tau_{180} = 10$ ms; the points of maximal refocusing are shifted significantly earlier in time than the SE times, and the monoexponential curve does not pass through them. Despite this offset, when at least three SEs from the CFS were fit to a monoexponential decay, the fitted ΔR_2 values were within 2% of those predicted by Equation [6] for the ranges $\tau_{180} = 1$–75 ms and $D = 0.5$–$4\,\mu m^2/ms$, as shown in Figure 3c. For the FID, it is evident from Figure 3a that the CFS initially
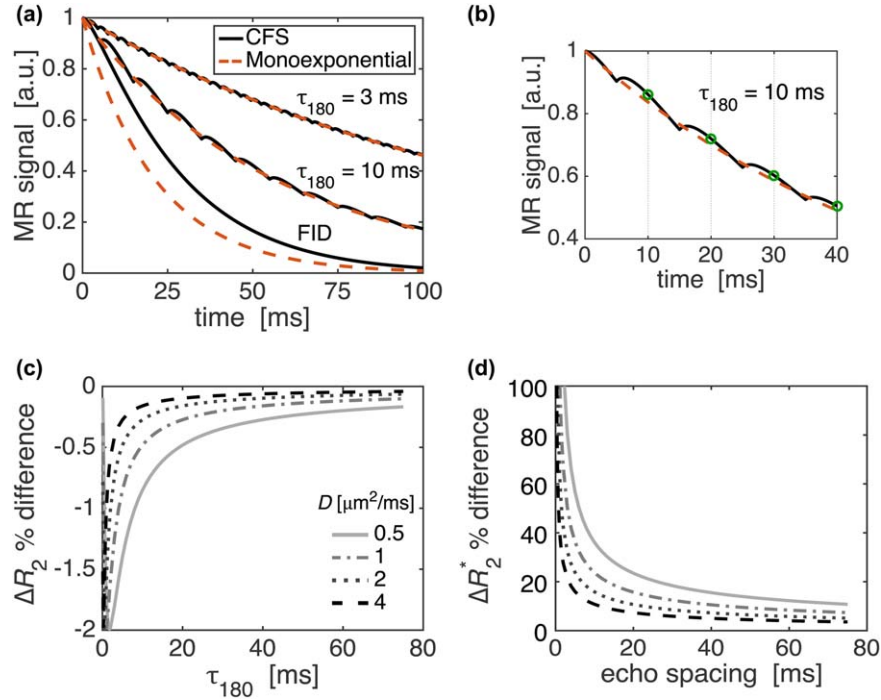
FIG. 3. Comparison of the CFS in Equation [9] versus the monoexponential approximation in Equation [6] from Jensen and Chandra (6), calculated for spheres simulating red blood cells in blood using $\zeta = 40\%$, $R = 3\,\mu m$, $D = 2\,\mu m^2/ms$, and $SO_2 = 60\%$, unless specified otherwise. **a**: Example time series for two τ_{180} values and for an FID. **b**: The $\tau_{180} = 10$ ms time series is expanded to highlight some of the characteristics of the CFS, such as the shift in the maximal refocusing points and the differences between it and the monoexponential approximation. (**b**) shares the same legend as (**a**), and the green markers represent the CFS signal at the spin-echo times. **c, d**: Percent differences between ΔR_2^* estimated from the monoexponential curve and the CFS shown for several diffusion coefficient values and as a function of echo spacing. **c**: Comparison of the CPMG signals where ΔR_2 from the CFS was estimated using three echoes. **d**: Comparison of the FID signals, in which ΔR_2^* from the CFS was estimated using 10 echoes. (**c**) and (**d**) share the same legend. ζ, volume fraction; R, radius; D, diffusion coefficient; SO_2, oxygen saturation.

diverges from monoexponential decay and gradually reaches it. Thus, values of ΔR_2^* from the monoexponential expression significantly overestimate the ΔR_2^* estimated using 10 echoes from the CFS, particularly at short echo spacings (Fig. 3d). A similar comparison of the signal evolution from multiple spheroid geometries is also given in the Supporting Information (see Supporting Fig. S2 and Supporting Table S1).

Ex Vivo Validation

Of the 31 samples that were analyzed, two of them had $T_{2,0}$ estimates that reached the upper bound in both the WFA fits, and one of these samples reached the upper bound in the LM-R_2 fit; both appeared to result from image quality issues and were excluded from the remaining analyses. Example fits of the three models to the same blood sample are shown in Figure 4. The fitted τ_D
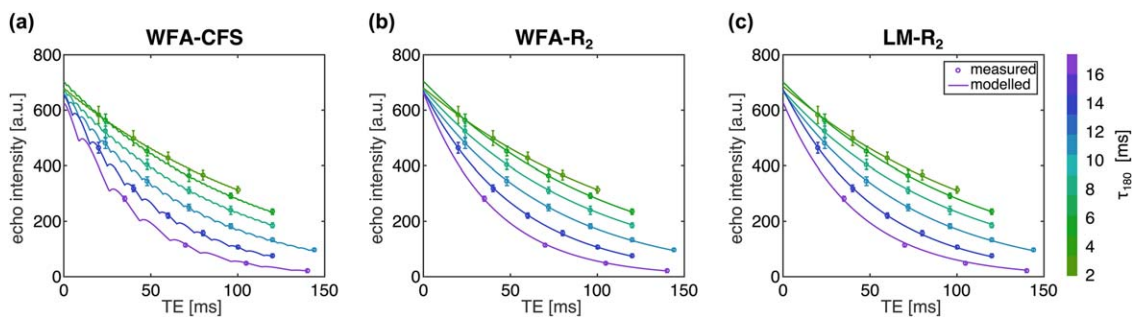
FIG. 4. Example fits from a single blood sample using the weak field approximation (WFA) CFS model (**a**), the WFA monoexponential model (WFA-R_2) (**b**), and the Luz-Meiboom monoexponential model (LM-R_2) (**c**). Mean signal intensities $\pm$ their standard deviations are displayed with the circle markers, and the model fits are plotted with the curves. Each color represents a different τ_{180} refocusing interval, labeled on the right. Data points are from a T_2-prepared sequence in which the preparation durations were varied by integer multiples of the τ_{180}; therefore, not every spin echo is sampled.
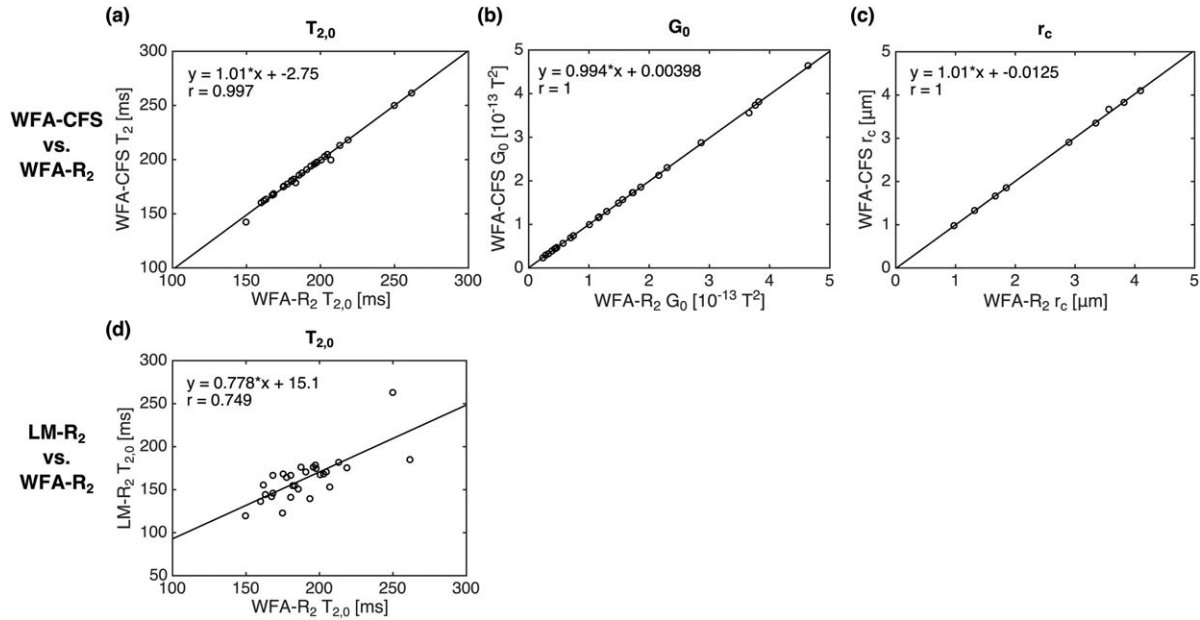
FIG. 5. Agreement between the fitted parameters from the WFA-CFS and WFA-R_2 models (top row) and the LM-R_2 and WFA-R_2 models (bottom row). $T_{2,0}$, G_0, and r_c are compared between the WFA models; however, only $T_{2,0}$ is compared between the monoexponential models, as the other parameters are not equivalent for comparison. Figure legends show the line of best-fit coefficients and the Pearson correlation coefficient, *r*.

values were converted to r_c using $\tau_D = r_c^2/D$, assuming $D = 1.4\ \mu m^2/ms$ in blood at 20 °C (7). Correlations among the individual fitted parameters were calculated using the Pearson correlation coefficient and are displayed in Figure 5. The mean fit parameters are summarized in Table 1. Statistical comparisons were made between the two WFA model fits (WFA-CFS and WFA-R_2) and between the two R_2-based model fits (WFA-R_2 and LM-R_2), where appropriate, using two-sided paired t-tests. The two WFA model fits were nearly identical, consistent with the theoretical CPMG results in Figure 3. The total sum of square residuals was lower for the WFA models than for the LM-R_2 model; however, this was not statistically significant.

DISCUSSION

In this study, we used the weak field approximation model to describe the entire transverse signal time course. To determine the dephasing regime in which the CFS was valid, we compared it with simulations in

which the sphere radii were increased from 0.9 up to 24 μm. In most of the pulse sequences, the CFS started to significantly overestimate the decay for $R > 3.2\ \mu m$, but was accurate at least up to this radius (see Fig. 2). The motional narrowing regime is most commonly classified using the dimensionless inequality $\alpha = \tau_D \delta\omega \ll 1$ (4). With our simulation parameters, a radius of 3.2 μm results in $\alpha = 2.7$, meaning that the WFA is valid in the motional narrowing regime, as expected, and it can be applied across the motional narrowing-intermediate dephasing regime boundary but not well beyond it. Both the simulations and the WFA modeled unrestricted diffusion; the deviations that arose between the two demonstrate the limitation of the WFA to predict transverse signal as the system transitions from the motional narrowing regime into the static dephasing regime. The deviations were likely greatest for the FID sequence since, because of the lack of refocusing pulses, the relaxation rates were larger than in the SE and CPMG sequences, allowing the simulated and predicted signals to diverge more.

Table 1

Fitted Model Parameters From the WFA Using Either the WFA-CFS or the WFA-R_2, or the LM-R_2

Parameter/Model	1. WFA-CFS	2. WFA-R_2	3. LM-R_2	t-test	
				$P(1\neq2)$[a]	$P(2\neq3)$[b]
Total SSR	186,563	186,522	187,897	0.1	0.7
$T_{2,0}$ (ms)	189 ± 25	190 ± 25	163 ± 26	0.08	<0.001
r_c (μm)	2.6 ± 1.2	2.6 ± 1.2	–	0.3	
G_0 ($10^{-13}\ T^2$)	1.5 ± 1.2	1.5 ± 1.2	–	0.1	
K_0 ($10^{-13}\ T^2$)	–	–	0.93 ± 0.98		
τ_{ex} (ms)	–	–	2.2 ± 0.8		

Note: Mean ± standard deviation model parameters are displayed. SSR, sum of square residuals.
[a]Paired t-tests are between the WFA Models 1 and 2.
[b]Paired t-tests are between the R_2 Models 2 and 3.

We found that the closed-form solution and the original WFA expression for monoexponential decay provided very similar estimates for ΔR_2 in CPMG sequences (Fig. 3). However, the discrepancy for the FID decay could be significant (up to as much as 100% error in the estimates of ΔR_2^*). In light of the agreement between the simulations and the CFS in the motional narrowing regime, as detailed in Figure 2, we attribute this discrepancy to the ΔR_2^* model not accurately accounting for the amount of time required for the FID to approach monoexponential decay. Considering that most multi-echo gradient-echo sequences use echo spacings less than 20 ms, the discrepancy could be substantial if one were to use measured ΔR_2^* values to obtain quantitative estimates of the underlying tissue properties.

These CPMG findings were echoed in the ex vivo relaxometry analysis, in which the WFA monoexponential and CFS fits gave nearly identical model parameters across a wide range of blood oxygenations. That the WFA models provided a slightly better fit than the LM model may indicate that the WFA model of diffusion more realistically describes the underlying relaxation mechanisms or that it can more flexibly adapt to the data. The WFA fits were more sensitive than the LM model fits to image quality issues. This may be an advantage for the LM model, but having sensitivity to image quality issues may also have its merits. In the preceding simulations, the CFS accurately predicted signal evolution in the motional narrowing regime, suggesting that the WFA should reliably fit the relaxometry data. Diffusion through field gradients has been shown to be the dominant source of transverse relaxation in suspensions of RBCs at 7 T (24); however, the WFA may become more biased at these higher field strengths. As the field strength is decreased, the relative contribution of chemical exchange to relaxation is expected to increase, as its contribution changes at a less than quadratic rate with respect to B_0, whereas the diffusion contribution is expected to change at a quadratic rate (25). That the results of the Luz-Meiboom exchange model fits gave an exchange time of 2.2 ms, whereas the exchange lifetime of water in RBCs is generally considered to be approximately 10 ms (26–29), is evidence that the LM chemical exchange model alone is insufficient to describe transverse relaxation at 3 T. This finding of lower than expected τ_{ex} is consistent with several earlier studies with B_0 of approximately 1.5 to 4.7 T (7–9,30–32). Invariably, both relaxation mechanisms contribute to T_2 decay, and to what extent is a complex issue that further underscores the limitations of describing the relaxation by a single mechanism.

The WFA assumes unrestricted diffusion (i.e., that the diffusion inside, outside, and across the perturbers is equal and represented by a single diffusion coefficient). However, intracellular diffusion will generally be less than extracellular diffusion as a result of diffusion restriction from cell membranes. Using a single apparent diffusion coefficient for all compartments should be an accurate representation at low perturber concentrations; however, as the perturber concentration increases, the apparent diffusion coefficient will decrease as diffusion will be hindered by the finite permeability of the perturbers. For RBCs, where water is exchanging relatively quickly across the RBC boundaries, the apparent diffusion coefficient may be approximated by the weighted sum of intra- and extracellular diffusion coefficients (33), and they both can be corrected for their increased tortuosities (29,33,34). For blood, the apparent diffusion coefficient may be in the range of 1.5 to 2.1 μm^2/ms (29,35). Using $\alpha = r_c^2/D\gamma\Delta\chi B_0/3$ and starting with the conditions $D = 1.5\,\mu m^2$/ms, $r_c = 2.6\,\mu m$ (from the ex vivo fits), $\Delta\chi = 1.2$ ppm (or $SO_2 = 60\%$), and $B_0 = 3$ T, gives $\alpha = 1.4$. One can then determine the conditions under which the theory will still be accurate ($\alpha \lesssim 2.7$). Either doubling the susceptibility offset or the field strength, increasing r_c by a factor of $\sqrt{2}$, or halving the diffusion coefficient will result in a doubling of α, thus putting it slightly over the threshold. The susceptibility offset may be altered either endogenously by decreasing SO_2 or exogenously by the administration of a contrast agent. These numbers serve as an estimate for the range of applicability and are sensitive to the assumed cell size and diffusion coefficient.

The simulated conditions, although framed primarily in the context of modeling blood, can also apply to signal from iron depositions in tissue. The combination of volume fraction, $\Delta\chi$, and B_0 strength simulated gave $G_0 = 4.3 \times 10^{-14}$ T^2, which is comparable to that in deep gray matter at 2.35 T (6), where G_0 and r_c were found to be approximately $(1–6) \times 10^{-14}$ T^2 and 2.3 to 3.1 μm, respectively. The diffusion coefficient, however, would be approximately 1.0 μm^2/ms, such that for iron depositions modeled by perturbers with $r_c = 2.6\,\mu m$ and the same G_0, α would equal 2.2. Given that the CFS was accurate up to $\alpha \approx 2.7$, this would imply that the WFA would likely lose accuracy for more severe iron deposition, field strengths greater than 3 T, larger cell sizes, or reduced diffusion. However, this may not preclude a more qualitative interpretation of the WFA parameters for iron imaging, whereby the r_c and G_0 estimates may be biased but still proportional to their true values.

A limitation of this study is that the in silico validation of the CFS was only performed using spherical perturbers. This was done since analytical solutions for G_0 and r_c had previously been derived, allowing the simulations to be predicted a priori. For other geometries, the parameters G_0 and r_c would take on other values, but they would scale with volume fraction and field offset strength similarly (5). In the Supporting Information, additional spheroid geometries were analyzed and the transverse signal predicted by the WFA was found to be in good agreement with the signal predicted by the geometry-specific Gaussian phase approximation. However, it may still be convenient to interpret in vivo or ex vivo relaxometry results as if the perturbers were spherical, as the exact shape of the cells may not be known a priori. Using the Gaussian phase approximation in the long time limit, Sukstanskii and Yablonskiy (5) calculated ΔR_2 for spheroids that were uniformly oriented relative to B_0. Even for the case of an oblate spheroid, in which one semi-axis is twice the length of the other, a geometry that has previously been used to represent RBCs (35), ΔR_2 would still be within 4% of that of spheres (when the sphere and spheroid volumes and

volume fractions are matched). This reflects how the extracellular field inhomogeneities from spheroids and RBCs can be approximated as those from a sphere (30). In the short time limit, relaxation is most sensitive to water molecules dephasing from exchanging across the perturber boundary, which depends on the perturber's surface area–to-volume ratio (5). This ratio for the oblate spheroid is approximately two-thirds that of a sphere's, so a sphere does not reliably reproduce the initial time course. Therefore, particularly in the long time limit, fits to the CFS for oblate spheroids could cautiously be interpreted as if they were spheres; however, this assumption of spherical perturbers can be avoided by using the correct expression for r_c, where possible. As demonstrated in the Supporting Information, the fitted r_c parameter may be valid for a range of spheroid geometries (spherical, oblate, and prolate), with the caveat that it may slightly underestimate the true r_c value.

The comparison of the WFA with the simulations, the Gaussian phase approximation, and the chemical exchange model informs us about the inherent differences between these models or the assumptions underlying the simulations. This is relevant in that none of these models explicitly account for other complex effects such as flow or the potential preferential alignment of RBCs or spheroids with the B_0 field (30). Although this orientation effect appears to only weakly affect the transverse relaxation (35) and is potentially diminished by flow itself (24), it may be useful to attempt to incorporate it into future modeling studies.

We envision the CFS could be used to simplify the simulation of transverse signal decay from systems in the motional narrowing regime, such as blood, where the sheer number of perturbers makes simulation a computational burden. This could be achieved by directly substituting the simulation time course with the CFS analytical time course, provided appropriate values for G_0 and r_c. When analytical solutions for G_0 and r_c are not apparent, these parameters could be empirically determined by fitting the radial correlation function of the system of perturbers using Equation [4]. Another application of the CFS could be to decrease the total scan time required for fitting transverse signal decay to the WFA by substituting the large number of refocusing rates used during a CPMG experiment with fewer refocusing rates and sampling the signal at time points away from the SE times. The non-SE samples would provide additional information related to the characteristic perturber size that could then be fit using the CFS. It may even be feasible to reduce the number of acquisitions to one with many gradient-echo readouts.

CONCLUSIONS

We have derived and validated a closed-form solution for transverse signal decay under a range of pulse sequences using the weak field approximation. Simulations were used to validate the CFS at time points away from SE times in FID, SE, and CPMG sequences. The CFS was found to be very accurate in the motional narrowing regime, as expected, and partially into the intermediate dephasing regime. A consequence of this is that the use of the WFA for brain tissue iron imaging may become increasingly biased at field strengths greater than 3 T. A more qualitative interpretation of those studies or use of an alternate theory developed for the intermediate or static dephasing regimes may be more appropriate.

When using CPMG signals at the SEs from the CFS to fit for ΔR_2, it was in excellent agreement with a well-known expression for asymptotic ΔR_2 derived in the original WFA study (6), showing self-consistency of the CFS within the WFA. This result was shown theoretically and experimentally with ex vivo blood CPMG data. This comparison also showed that the time for an FID to approach monoexponential decay can be substantial; therefore, gradient echo data should be fit using the CFS rather than the monoexponential form of the WFA.

Overall, this study has advanced the biophysical signal modeling from tissues in nonstandard CPMG sequences. This could help simplify simulations from tissues such as blood, or reduce the amount of time required for quantitative in vivo or ex vivo MR acquisitions from systems in the motional narrowing regime.

REFERENCES

1. Yablonskiy DA, Haacke EM. Theory of NMR signal behavior in magnetically inhomogeneous tissues: the static dephasing regime. Magn Reson Med 1994;32:749–763.
2. Wehrli FW, Song HK, Saha PK, Wright AC. Quantitative MRI for the assessment of bone structure and function. NMR Biomed 2006;19: 731–764.
3. Carr HY, Purcell EM. Effects of diffusion on free precession in nuclear magnetic resonance experiments. Phys Rev 1954;94:630–638.
4. Gillis P, Koenig SH. Transverse relaxation of solvent protons induced by magnetized spheres: application to ferritin, erythrocytes, and magnetite. Magn Reson Med 1987;5:323–345.
5. Sukstanskii AL, Yablonskiy DA. Gaussian approximation in the theory of MR signal formation in the presence of structure-specific magnetic field inhomogeneities. J Magn Reson 2003;163:236–247.
6. Jensen JH, Chandra R. NMR relaxation in tissues with weak magnetic inhomogeneities. Magn Reson Med 2000;44:144–156.
7. Chen JJ, Pike GB. Human whole blood T2 relaxometry at 3 Tesla. Magn Reson Med 2009;61:249–254.
8. Stefanovic B, Pike GB. Human whole-blood relaxometry at 1.5 T: assessment of diffusion and exchange models. Magn Reson Med 2004;52:716–723.
9. Gardener AG, Francis ST, Prior M, Peters A, Gowland PA. Dependence of blood R2 relaxivity on CPMG echo-spacing at 2.35 and 7 T. Magn Reson Med 2010;64:967–974.
10. Jensen JH, Chandra R, Ramani A, Lu H, Johnson G, Lee SP, Kaczynski K, Helpern JA. Magnetic field correlation imaging. Magn Reson Med 2006;55:1350–1361.
11. Wismer GL, Buxton RB, Rosen BR, Fisel CR, Oot RF, Brady TJ, Davis KR. Susceptibility induced MR line broadening: applications to brain iron mapping. J Comput Assist Tomogr 1988;12:259–265.
12. Yablonskiy DA, Haacke EM. An MRI method for measuring T2 in the presence of static and RF magnetic field inhomogeneities. Magn Reson Med 1997;37:872–876.
13. Ma J, Wehrli FW. Method for image-based measurement of the reversible and irreversible contribution to the transverse-relaxation rate. J Magn Reson B 1996;111:61–69.

14. Storey P, Chung S, Ben-Eliezer N, Lamberskiy G, Lui YW, Novikov DS. Signatures of microstructure in conventional gradient and spin echo signals. 2015; Toronto. In Proceedings of the 23rd Annual Meeting of ISMRM, Toronto, Canada, 2015. p. 14.

15. Berman AJ, Pike GB. A general solution for transverse signal decay under the weak field approximation: theory and validation with spherical perturbers. 2016; Singapore. In Proceedings of the 24th Annual Meeting of ISMRM, Singapore, 2016. p. 506.

16. Kiselev VG, Novikov DS. Transverse NMR relaxation as a probe of mesoscopic structure. Phys Rev Lett 2002;89:278101.

17. Klassen LM, Menon RS. NMR simulation analysis of statistical effects on quantifying cerebrovascular parameters. Biophys J 2007;92:1014–1021.

18. Pannetier NA, Sohlin M, Christen T, Schad L, Schuff N. Numerical modeling of susceptibility-related MR signal dephasing with vessel size measurement: phantom validation at 3T. Magn Reson Med 2014;72:646–658.

19. Spees WM, Yablonskiy DA, Oswood MC, Ackerman JJ. Water proton MR properties of human blood at 1.5 Tesla: magnetic susceptibility, T(1), T(2), T*(2), and non-Lorentzian signal behavior. Magn Reson Med 2001;45:533–542.

20. Berman AJ, Ma Y, Hoge RD, Pike GB. The effect of dissolved oxygen on the susceptibility of blood. Magn Reson Med 2016;75:363–371.

21. Luz Z, Meiboom S. Nuclear magnetic resonance study of protolysis of trimethylammonium ion in aqueous solution - order of reaction with respect to solvent. J Chem Phys 1963;39:366–370.

22. Weisskoff RM, Zuo CS, Boxerman JL, Rosen BR. Microscopic susceptibility variation and transverse relaxation: theory and experiment. Magn Reson Med 1994;31:601–610.

23. Yablonskiy DA, Sukstanskii AL, He X. Blood oxygenation level-dependent (BOLD)-based techniques for the quantification of brain hemodynamic and metabolic properties—theoretical models and experimental approaches. NMR Biomed 2013;26:963–986.

24. Gasparovic C, Matwiyoff NA. The magnetic properties and water dynamics of the red blood cell: a study by proton-NMR lineshape analysis. Magn Reson Med 1992;26:274–299.

25. Matwiyoff NA, Gasparovic C, Mazurchuk R, Matwiyoff G. The line shapes of the water proton resonances of red blood cells containing carbonyl hemoglobin, deoxyhemoglobin, and methemoglobin: implications for the interpretation of proton MRI at fields of 1.5 T and below. Magn Reson Imaging 1990;8:295–301.

26. Thulborn KR, Waterton JC, Matthews PM, Radda GK. Oxygenation dependence of the transverse relaxation time of water protons in whole blood at high field. Biochim Biophys Acta 1982;714:265–270.

27. Benga G, Borza V, Popescu O, Pop VI, Muresan A. Water exchange through erythrocyte membranes: nuclear magnetic resonance studies on resealed ghosts compared to human erythrocytes. J Membr Biol 1986;89:127–130.

28. van Zijl PC, Eleff SM, Ulatowski JA, Oja JM, Ulug AM, Traystman RJ, Kauppinen RA. Quantitative assessment of blood flow, blood volume and blood oxygenation effects in functional magnetic resonance imaging. Nature Med 1998;4:159–167.

29. Stanisz GJ, Li JG, Wright GA, Henkelman RM. Water dynamics in human blood via combined measurements of T2 relaxation and diffusion in the presence of gadolinium. Magn Reson Med 1998;39:223–233.

30. Gillis P, Peto S, Moiny F, Mispelter J, Cuenod CA. Proton transverse nuclear magnetic relaxation in oxidized blood: a numerical approach. Magn Reson Med 1995;33:93–100.

31. Ye FQ, Allen PS. Relaxation enhancement of the transverse magnetization of water protons in paramagnetic suspensions of red blood cells. Magn Reson Med 1995;34:713–720.

32. Portnoy S, Osmond M, Zhu MY, Seed M, Sled JG, Macgowan CK. Relaxation properties of human umbilical cord blood at 1.5 Tesla. Magn Reson Med 2017;77:1678–1690.

33. Szafer A, Zhong J, Gore JC. Theoretical model for water diffusion in tissues. Magn Reson Med 1995;33:697–712.

34. Nicholson C, Phillips JM. Ion diffusion modified by tortuosity and volume fraction in the extracellular microenvironment of the rat cerebellum. J Physiol 1981;321:225–257.

35. Wilson GJ, Springer CS Jr, Bastawrous S, Maki JH. Human whole blood 1 H2 O transverse relaxation with gadolinium-based contrast reagents: magnetic susceptibility and transmembrane water exchange. Magn Reson Med 2017;77:2015–2027.

SUPPORTING INFORMATION

Additional Supporting Information may be found in the online version of this article.

Fig. S1. (**a, c**) Comparison of the exact temporal correlation function for spheroids from the Gaussian phase approximation (GPA, black line) and the algebraic temporal correlation function from the WFA (dashed red line). The correlation functions have been normalized by the mean square field inhomogeneity, G_0, and time has been normalized by the characteristic diffusion time, $t_c = r_c^2/D$. The percent differences between the two are shown in (**d**) to (**f**), using the exact correlation function as the reference.

Fig. S2. Comparison between the Gaussian phase approximation (GPA, circles), the WFA CFS (dashed lines), and the r_c-optimized WFA CFS (solid lines) for the FID (red) and spin-echo time courses (black). The nonoptimized WFA line colors are less saturated to improve visual contrast.

Table S1. Agreement of the WFA-CSF With the Exact FID and Spin-Echo Signal Decay of the Gaussian Phase Approximation

Note: In the third column, r_c was scaled to minimize the RMSE, with the scaling factor given in the last column.

Supporting Information

Transverse signal decay under the weak field approximation: theory and validation

Avery J.L. Berman and G. Bruce Pike

In this study, the closed-form solution (CFS) for the weak field approximation (WFA) was validated against simulations from populations of spherical perturbers. To investigate how well the WFA may apply to other geometries, here we consider the temporal correlation functions and transverse signal evolutions of ellipsoids of revolution, for which Sukstanskii and Yablonskiy have derived exact analytical expressions under the Gaussian phase approximation (GPA) (1). Oblate spheroids have previously been used to model red blood cells, hence, these geometries also have biological relevance (2).

Temporal Correlation Functions

Under the WFA of Jensen and Chandra (3), a generic temporal correlation function, given by the algebraic expression reproduced in Eq. [5] of the main text, was proposed. That expression is

$$K_{WFA}(t) = G_0 \left(1 + \frac{4Dt}{r_c^2}\right)^{-\frac{3}{2}}, \qquad [S1]$$

where G_0 is the mean square field inhomogeneity (in units of T^2), D is the diffusion coefficient, and r_c is the characteristic length – dependent on perturber geometry. Jensen and Chandra also derived an exact temporal correlation function for spheres and found that it and the algebraic function were in excellent agreement (3).

In the GPA, the exact temporal correlation functions for several geometries were derived, including those for spheres and spheroids. Spheroids are defined as rotated ellipses with semi-axes a and b, with the b-axis being the axis of rotation. This describes a sphere when $a = b$, a flattened sphere when $a > b$ (known as an oblate spheroid), and a rugby ball shape when $a < b$ (known as a prolate spheroid). The temporal correlation function for spheroids that are uniformly distributed throughout the system volume and uniformly oriented is (1)

$$K_{GPA}(t) = \frac{6G_0}{\pi} \int_0^\infty du\, u \int_0^\infty dv\, \exp\left(-\frac{tu^2}{t_a} - \frac{tv^2}{t_b}\right)$$

$$\cdot \frac{(\sin\tilde{q} - \tilde{q}\cos\tilde{q})^2}{\tilde{q}^6}, \quad \tilde{q} = (u^2 + v^2)^{1/2}$$

[S2]

where $t_a = a^2/D$, $t_b = b^2/D$. Note, the notation has been modified slightly to be consistent with that used in this paper, i.e., G_0 is in units of T^2 rather than s^{-2}, and G_0 is given by Eq. [11] in both cases. The long-time limit of $K(t)$ for ellipsoids, when $t \gg t_a$ and $t \gg t_b$, was shown to be

$$K_{GPA}(t) \cong \frac{G_0}{6\sqrt{\pi}} \frac{a^2 b}{(Dt)^{3/2}}.$$

[S3]

By making the substitution $b = \lambda a$ and equating the long-time behaviour of K_{WFA} and K_{GPA}, it can be shown that the characteristic length is related to a and λ by

$$r_c = \left(\frac{4\lambda}{3\sqrt{\pi}}\right)^{\frac{1}{3}} a.$$

[S4]

This simplifies to Eq. [10] when $\lambda = 1$ (i.e., $b = a$).

Comparisons of the WFA and exact temporal correlation function of the GPA in Eqs. [S1] and [S2], respectively, for spheres, oblate spheroids ($\lambda = 0.5$), and prolate spheroids ($\lambda = 2$) are shown in Sup. Fig. S1. The case where $\lambda = 0.5$ has previously been used to model red blood cells with $a = 4$ μm and $b = 2$ μm (2). Eq. [S2] was computed by numerical integration in MATLAB. At short times, large percent differences between the correlation functions develop for all three examples, with $\lambda = 1$ showing the smallest difference in magnitude and extent in time. The time to return to below 5% difference is approximately $0.25t_c$ for $\lambda = 1$, t_c for $\lambda = 0.5$, and $1.33t_c$ for $\lambda = 2$.
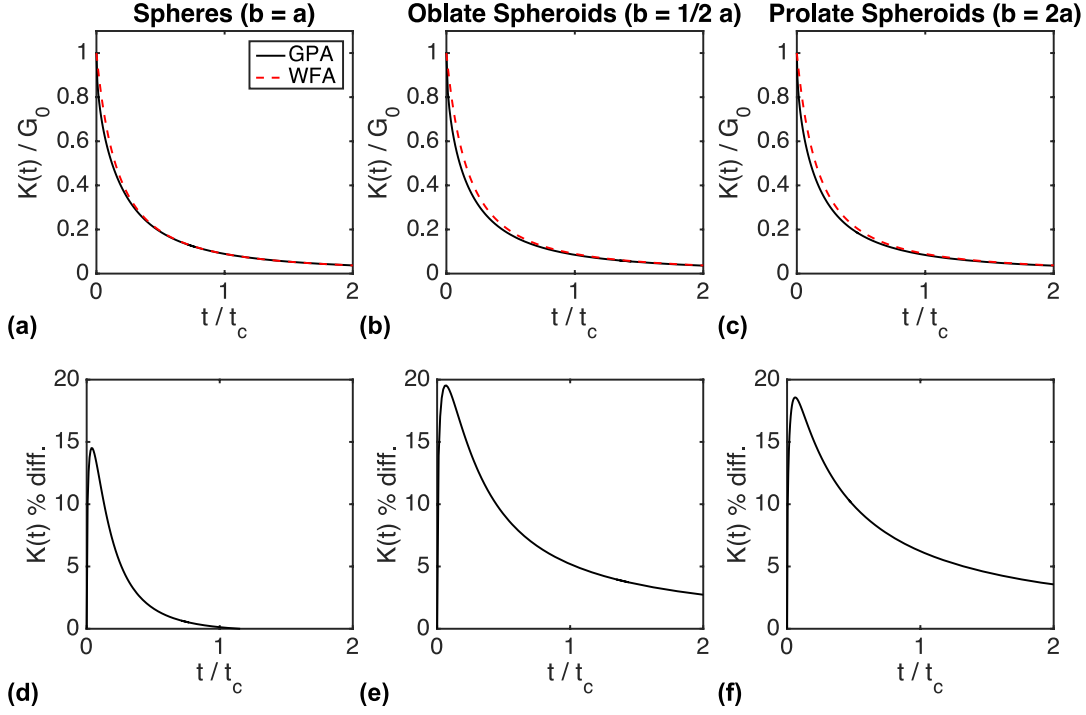
Supporting Figure S1: (a)–(c) Comparison of the exact temporal correlation function for spheroids from the Gaussian phase approximation (GPA, black line) and the algebraic temporal correlation function from the weak field approximation (WFA, dashed red line). The correlation functions have been normalized by the mean square field inhomogeneity, G_0, and time has been normalized by the characteristic diffusion time, $t_c = r_c^2/D$. The percent differences between the two are shown in (d)–(f), using the exact correlation function as the reference.

Transverse Signal Evolution

Using the correlation function in Eq. [S2], Sukstanskii and Yablonskiy derived analytic expressions to describe the transverse signal evolution from spheroids (1). Both the FID and SE signal intensities are described by the equation

$$S_{GPA}(t) = \exp\left[-\frac{6G_0}{\pi}\int_0^\infty du\, u\, \int_0^\infty dv\, \frac{(\sin\tilde{q} - \tilde{q}\cos\tilde{q})^2}{\tilde{q}^6}\right.$$
$$\left. \cdot g\left(\frac{u^2}{t_a} + \frac{v^2}{t_b}, t\right)\right],$$

[S5]

where $g(x,t)$ is defined separately for FID and SE sequences as

$$g_{FID}(x,t) = \frac{1}{x^2}(e^{-xt} + xt - 1),$$

$$g_{SE}(x,t) = \frac{1}{x^2}\left(4e^{-xt/2} - e^{-xt} + xt - 3\right).$$

[S6]

Examples of this exact expression from the GPA are compared against the WFA CFS in Sup. Fig. S2. Eq. [S5] was computed by numerical integration. In all three cases, the semi-axes were chosen to give the same r_c value: $b = a = 3$ μm for spheres, $b = 1/2 \, a = 1.89$ μm for prolate spheroids, and $b = 2a = 4.76$ μm for oblate spheroids, all resulting in $r_c = 2.73$ μm using Eq. [S4]. All other simulation settings matched those from Figure 3, i.e., $\zeta = 40\%$, $D = 2$ μm^2/ms, $SO_2 = 60\%$, and $B_0 = 3$ T. The combined FID and SE root mean square error (RMSE) between the CFS and the GPA are listed in Sup. Table S1. The WFA r_c parameter was then scaled to minimize the RMSE between the CFS and the GPA signals using non-linear least squares minimization. This is plotted in Figure S2 and listed in Table S1.
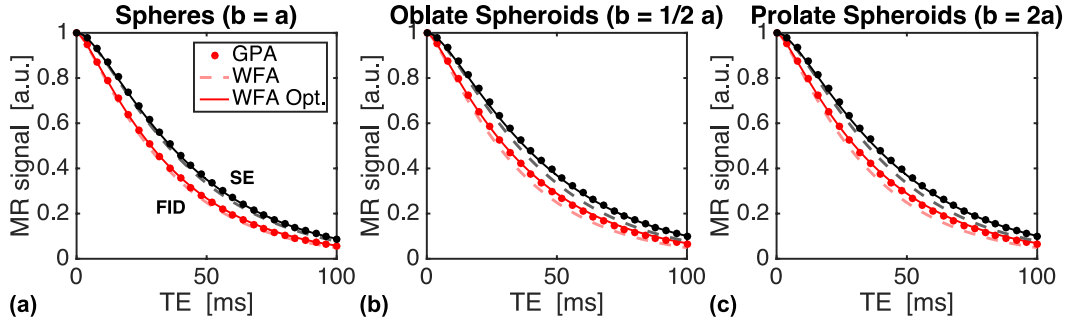
Supporting Figure S2: Comparison between the Gaussian phase approximation (GPA, circles), the WFA closed-form solution (dashed lines), and the r_c-optimized WFA CFS (solid lines) for the FID (red) and SE time courses (black). The non-optimized WFA line colours are less saturated to improve visual contrast.

Supporting Table S1: Agreement of the WFA closed-form solution with the exact FID and SE signal decay of the Gaussian phase approximation. In column three, r_c was scaled to minimize the root mean square error (RMSE) – with the scaling factor given in the last column.

Geometry	RMSE – initial	RMSE – optimized	r_c scaling
Spheres	0.0142	0.00360	0.969
Oblate spheroids	0.0297	0.00612	0.938
Prolate spheroids	0.0300	0.00590	0.937

The differences between the WFA and the GPA signals are minimal for spheres but more apparent for the two other spheroid shapes. This is consistent with the r_c scaling used to minimize the RMSE, which was only 0.97 for spheres but 0.94 for both spheroids. This scaling would suggest that r_c estimates from in vivo or ex vivo tissue may *slightly* underestimate the true r_c value if the perturbers can be described by a spheroid geometry; however, the overall agreement between the CFS and the exact Gaussian phase approximation solution is very good for multiple spheroid geometries.

References

1. Sukstanskii AL, Yablonskiy DA. Gaussian approximation in the theory of MR signal formation in the presence of structure-specific magnetic field inhomogeneities. J Magn Reson 2003;163(2):236-247.

2. Wilson GJ, Springer CS, Jr., Bastawrous S, Maki JH. Human whole blood 1 H2 O transverse relaxation with gadolinium-based contrast reagents: Magnetic susceptibility and transmembrane water exchange. Magn Reson Med 2017;77(5):2015-2027.

3. Jensen JH, Chandra R. NMR relaxation in tissues with weak magnetic inhomogeneities. Magn Reson Med 2000;44(1):144-156.